Sensitivity of a Global Forecast Model to Initializations with Reanalysis Datasets

GONZALO MIGUEZ-MACHO AND JAN PAEGLE

Department of Meteorology, University of Utah, Salt Lake City, Utah

(Manuscript received 14 April 1999, in final form 21 March 2000)

ABSTRACT

A global research model is initialized with reanalysis datasets obtained from NCEP and ECMWF. The globally averaged accuracy of the resulting 120-h predictions varies little between the different initializations, but a perceptible difference arises in the mid- to high latitudes of the Southern Hemisphere, where ECMWF initialized forecasts have somewhat greater skill. Most of this benefit is explained by differences of the longer-wave components (wavenumbers 0–15) of the initial data. This motivates further diagnoses of globally computed sensitivity measures to initial data changes. Approximately 67% of the 120-h forecast difference produced by changing initial data from ECMWF to NCEP reanalyses is due to initial changes only in wavenumbers 0–15, and more than 85% of this difference is produced by initial changes in wavenumbers 0–20. The result implies downscale uncertainty growth and contradicts several recent predictability investigations based upon singular vector analyses, which emphasize upscale uncertainty growth. The results do not imply that singular vector analyses are in error. They only suggest that large-scale errors of the initial state may play a more prominent role than suggested in some singular vector analyses. Downscale uncertainty evolution may be due to greater analysis uncertainty at large spatial scales than considered in prior recent studies emphasizing upscale predictability loss.

1. Introduction

Thompson (1957) presented one of the earliest and most frequently quoted references on atmospheric predictability. That work was based upon a nondivergent barotropic model, and concluded that the predictability of a given scale of the atmospheric circulation depends more sensitively upon initial state uncertainties of relatively larger scales than upon initial state uncertainties of relatively smaller scales. This result was later confirmed by Lorenz (1969, p. 296) and implies downscale uncertainty transfer in barotropic models.

The conclusion has a clear physical interpretation for the nondivergent barotropic case, which determines flow evolution from vorticity conservation. Vorticity changes of this model are strongly influenced by transport from one place to another, and advection dominates this evolution. A given wave component is systematically advected over distances on the order of, or longer than, its own wavelength only by longer scales. Uncertainty in longer scales produces similar advective placement errors in all sufficiently smaller scales, but the relative phase errors are larger for smaller scales and wave phase errors are consequently proportional to wavenumber. This leads to a second fundamental conclusion from barotropic reasoning, that the predictability of a given scale of motion is inversely proportional to its wavelength.

Lorenz's (1969) barotropic analysis suggests that long waves may exhibit predictability for a few weeks, synoptic scales may be predictable for a few days, mesoscales for a few hours, and small scales for a few minutes. A large number of global primitive equation model simulations support this general conclusion, at least for global- and synoptic-scale motions (e.g., Charney et al. 1966; Smagorinsky 1969; Williamson and Kasahara 1971; Kasahara 1972; Van Den Dool and Saha 1990; Reynolds et al. 1994). Lorenz's (1969) linear analyses retained many scales of motion, spanning several orders of magnitude. This degree of scale variability is still not affordable in uniform resolution global models, but one real-data, variable-resolution, global barotropic treatment, covering wavelengths from a few tens of kilometers to 40 000 km (Paegle et al. 1997) is consistent with Lorenz's (1969) analysis.

Paegle et al. (1997) present idealized integrations with multilevel baroclinic models imposing a global-scale wind uncertainty of magnitude 1 m s^{-1}. They demonstrate that this provokes stronger advective error growth rates than do errors associated with uncertain local triggering of pronounced baroclinic instability. This implies that slightly uncertain advective processes may dominate even strongly baroclinic situations, but no justifi-

Corresponding author address: Dr. Jan Paegle, Department of Meteorology, University of Utah, 135 S. 1460 E., Rm. 819, Salt Lake City, UT 84112-0110.
E-mail: jpaegle@atmos.met.utah.edu

cation was provided for the selected uncertainty magnitudes.

More recent predictability studies emphasize adjoint methods (e.g., Errico and Vukicevic 1992) and singular vector analyses (e.g., Buizza and Palmer 1995). Singular vectors are designed to optimize growth of some measure of the forecast field or of the forecast sensitivity, and they can be ordered according to their relative contributions to the total growth rate. The singular vectors are not shape preserving and commonly exhibit upscale energy growth. Singular vector analyses can be applied to time evolution of initial state uncertainties, and may quantify the ''butterfly effect'' (Lorenz 1993) for cases of upscale uncertainty growth (e.g., see discussion by Palmer et al. 1998).

Adjoint, or singular vector, analyses of error growth or predictability loss depend sensitively upon the measure or metric used to judge uncertainty growth. Palmer et al. (1998) show that metrics founded upon total energy of the initial state emphasize small-scale aspects of initial state uncertainty, and this conclusion is confirmed by Hartmann et al. (1995). The latter study performs a spherical harmonic decomposition and demonstrates that the top half (short-wave portion) of the leading singular vectors optimized in an energy metric explains most of their subsequent evolution.

Upscale error growths of singular vectors clearly produce a distinct error spectrum from that characterizing the downscale influences of erroneous advection rates. The scale dependence of related conclusions, however, depends strongly upon the measure or metric that is used in adjoint analysis. Singular vectors based upon an enstrophy metric at initial time emphasize large-scale components of the initial state uncertainty (Palmer et al. 1998), as do adjoint methods using local vorticity measures (Middlestadt 1995). Such singular vector analyses are consistent with downscale accentuation of error growth that characterizes uncertain advective processes.

Vukicevic (1998) demonstrates that the optimal initial perturbation approach does not offer a unique way to describe the initial development of observed cyclones. Singular vector analyses also present different answers that are dependent upon the imposed measures.

The problem of forecast error growth is essentially defined by the spectrum of initial state errors. If the most important errors are in long waves, then downscale error growth dominates. If the most important errors are in shorter scales, then upscale error growth may dominate uncertainty evolution.

In the absence of a known error spectrum, conjectures must be used. Palmer et al. (1998) use two separate analyses, both produced by the European Centre for Medium-Range Weather Forecasts (ECMWF) analysis system, of the same states to conclude that smaller-scale components of the initial state are more uncertain than longer-wave contributions. This provides the basis for their conjecture that the total energy metric at initial time is most suitable for singular vector calculations because the spectra of the dominant singular vectors are consistent with spectra of estimates of analysis error variance and this leads to upscale uncertainty growth. Barkmeijer et al. (1999) use the analysis error covariances implicit in a 3D-VAR data assimilation scheme as a surrogate for the actual analysis error covariances; the implied 3D-VAR covariances depend on the observation locations and error covariances as well as the time-averaged statistics of differences between model forecasts. This produces singular vectors whose dominant contributions are around global wavenumber 10.

The present study adds to this conjectural base. We use separate analyses provided by ECMWF and the National Centers for Environmental Prediction (NCEP) reanalyses to estimate initial state uncertainty, initialize the global Utah model with these data, and study the scale dependence of error growth through decomposition of the initial state uncertainty into spherical harmonics truncated at different global wave groups. The data are described in section 2. The model and its error characteristics are discussed in section 3, the scale dependence of uncertainty evolution is presented in section 4, and conclusions are summarized in section 5.

2. Datasets

NCEP (Kalnay et al. 1996) and ECMWF (Gibson et al. 1997) have performed gridded retrospective analyses, based upon assimilation of all available observations by a frozen state-of-the-art global data assimilation system. Our estimates of initial state uncertainty are obtained from the difference of these two equally credible analyses.

We select 17 cases, at 5-day intervals, starting on 1 January 1993 for model initialization. These particular dates are chosen because 8-day predictions by the version of the Medium Range Forecast (MRF) model used in the reanalysis project are available within the reanalysis archive. Those forecasts are available for the same 17 dates used in the Utah model initialization and allow comparison of the experimental model against a modern global forecast model (see next section).

Figure 1 presents midtropospheric rms differences between the NCEP and ECMWF reanalyses for the 17 selected cases. Height (wind) differences are on the order of 15–20 m (5 m s^{-1}) over the oceans. The differences increase in the Southern Hemisphere and become substantially larger over the Antarctic. Root-mean-square differences are smaller over regions of relatively dense rawinsonde coverage of North America, Europe, and much of Asia, suggesting convergence of the separate reanalyses in regions of higher observation density.

Figure 2 displays rms values of differences between NCEP and ECMWF reanalyses truncated at global wavenumber 15 of a spherical harmonic expansion. These show smoother patterns than Fig. 1, with somewhat smaller peak values, particularly for wind.

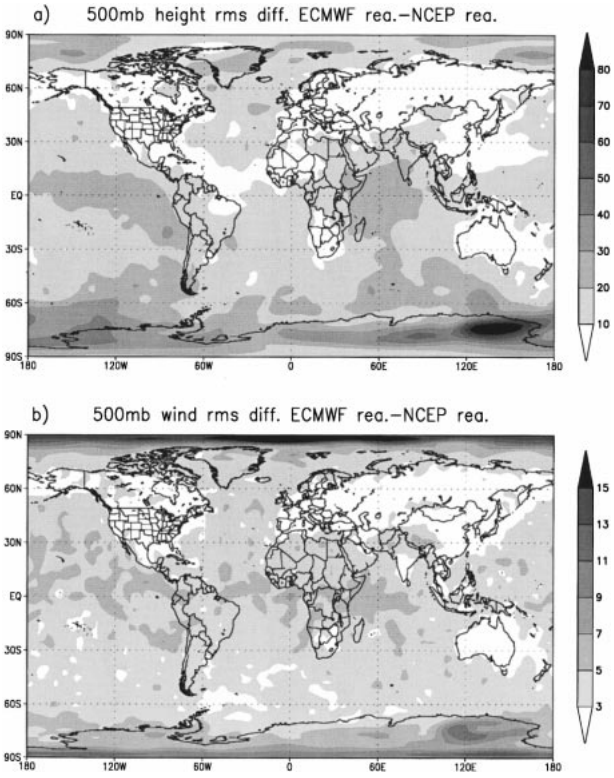

FIG. 1. Initial state 500-mb (a) geopotential heights and (b) wind rms differences between the NCEP and ECMWF reanalyses for the 17 selected cases. The units are (a) m and (b) m s^{-1}.

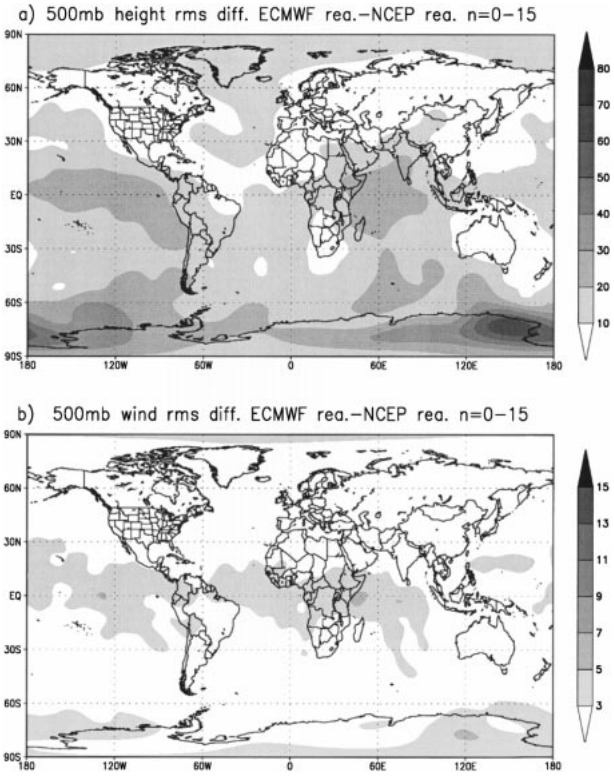

FIG. 2. Initial state 500-mb (a) geopotential heights and (b) wind rms differences between the NCEP and ECMWF reanalyses truncated at global wavenumber 15 for the 17 selected cases. The units are (a) m and (b) m s^{-1}.

The next section shows that errors in forecasts from the Utah model are slightly larger when the model is initialized with NCEP reanalysis data than when it is initialized with ECMWF reanalysis data. It is not clear whether this is due to sampling fluctuations and the small 17-case sample, to possible superiority of ECMWF analysis techniques, or to a slightly better match of that data with the Utah forecast model. Closer examination suggests that the relative forecast benefits are due mainly to superior ECMWF treatment of the high latitudes of the Southern Hemisphere, and might be produced by an assimilation error in the NCEP archive. Subsequent model error characteristics are estimated using ECMWF reanalyses to characterize the ''true'' observed state. Conclusions are largely unchanged if NCEP reanalyses are used to define ''truth.''

3. Model

The model used for this study is a multilevel, baroclinic version of the global model described by Paegle (1989). This hydrostatic model predicts vorticity, divergence, thermal, and moisture fields on pressure-based σ coordinates. The approach is similar to that used by global models in operational and research centers, with the exception of numerical approximations of horizontal derivatives, which are based on Fourier series in longitude and finite elements in latitude. Model physical parameterizations of convective and stable precipitation are similar to those used by the 1987 version of the National Center for Atmospheric Research Community Climate Model. Vertical mixing coefficients are calculated from a low-order turbulent energy equation that predicts turbulent kinetic energy, and radiative processes include cloud–radiation interactions, as described for another model by Nicolini et al. (1993). The present integrations retain nodal spacing 2.22° in latitude and 42 waves in longitude on 20 vertical levels, situated at σ = 0.99, 0.98, 0.96, 0.94, 0.91, 0.88, 0.84, 0.78, 0.72, 0.66, 0.59, 0.53, 0.47, 0.41, 0.34, 0.28, 0.22, 0.16, 0.09, and 0.03.

The model is initialized using temperature, wind, moisture, and surface pressure obtained from NCEP and ECMWF reanalyses. The NCEP archive also includes surface pressure, while the ECMWF archive gives only pressure adjusted to sea level. All model forecasts use surface pressure and elevation as given by the NCEP model in order to minimize surface imbalances that could result from a possibly inconsistent hypsometric adjustment of sea level pressure to model surface. This procedure should also minimize the relative impact of certain low-level analysis errors in NCEP reanalyses (see section 4, below). Experiments initialized with

ECMWF reanalyses use temperature, wind, and moisture fields from that analysis, but all surface conditions, including surface pressure and geopotential height, from NCEP reanalyses. Selected test cases show that use of ECMWF surface conditions produces insignificant differences in forecast accuracy.

Forecast error

1) GLOBAL ERRORS

The Utah model was originally designed by Paegle (1989) to address predictability questions. It has been used to study the impact of wind data voids on objective analyses (Paegle and Horel 1991), for predictability studies (Vukicevic and Paegle 1989; Paegle et al. 1997), for idealized global simulations of tropical–extratropical interactions (Buchmann et al. 1995), to study topographically forced regional circulations (Nogués-Paegle et al. 1998), and for predictability studies of the 1993 ''superstorm'' (Miguez-Macho and Paegle 1999a,b). The latter studies present error structure for March 1993, including the special case of the superstorm, and Wang et al. (1999) describe model accuracy for rainfall simulation. Errors relative to operational forecast models have not been previously documented. This is the first goal of the present section.

Figure 3 displays the 17-case, globally averaged vertical structure of 120-h rms temperature and meridional wind errors of the Utah model initialized with NCEP reanalyses (open circles), ECMWF reanalyses (closed circles), and of the MRF (open squares). The MRF clearly produces the best forecasts. This is not surprising since the MRF model is truncated at wavenumber 62 (instead of 42 as for the Utah model) and retains six more vertical levels. Additionally, the MRF has a longer history of development and calibration to real-data settings.

Closer inspection of the Utah model bias reveals systematically warm conditions at low levels over land surfaces covered by ice and snow and other locations characterized by low surface absorptivity of solar radiation. Those errors could be reduced by accounting for surface snow and other land surface characteristics that are not included by present model surface absorptivity specification, which distinguishes only the basis of surface elevation with respect to sea level. Errors can also be partly reduced by a posteriori extraction of the model bias, which produces vertical error structures depicted in Fig. 4.

Figure 5a displays the 17-case, globally averaged anomaly correlations of the 500-mb height field for the Utah model initialized with NCEP (open circles) and ECMWF (closed circles) reanalyses and for the MRF (open squares). Anomaly correlations for forecast variable S are calculated from

$$\text{anom. corr.} = \frac{\overline{(S - S_{\text{cl}})(S_{\text{ob}} - S_{\text{cl}})}}{[\overline{(S - S_{\text{cl}})^2}\,\overline{(S_{\text{ob}} - S_{\text{cl}})^2}]^{1/2}},$$

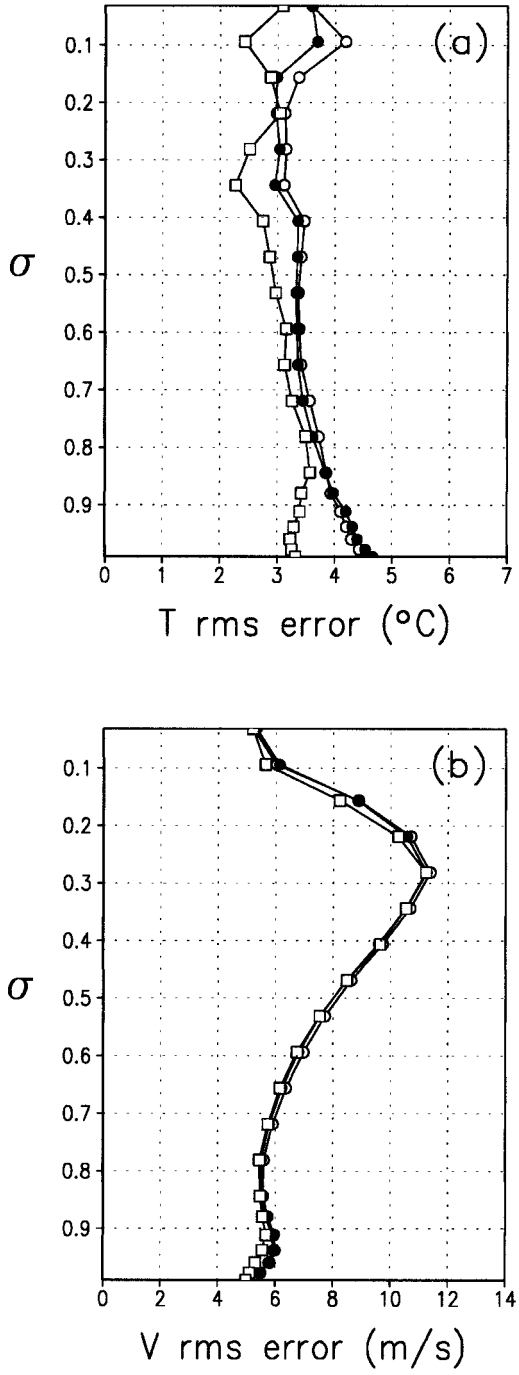

FIG. 3. Global, case-averaged vertical profiles of the 120-h rms errors with respect to ECMWF reanalysis, for (a) temperature and (b) meridional wind, of the Utah model initialized with NCEP reanalysis (open circles), ECMWF reanalysis (closed circles), and of the MRF (open squares). The units are (a) °C and (b) m s^{-1}.

where S_{cl} represents the climatological value of the variable S and S_{ob} the observed value, in this case from the ECMWF reanalysis. Here, $\overline{(\cdot)}$ indicates global area average.

The average for the months of January, February, and

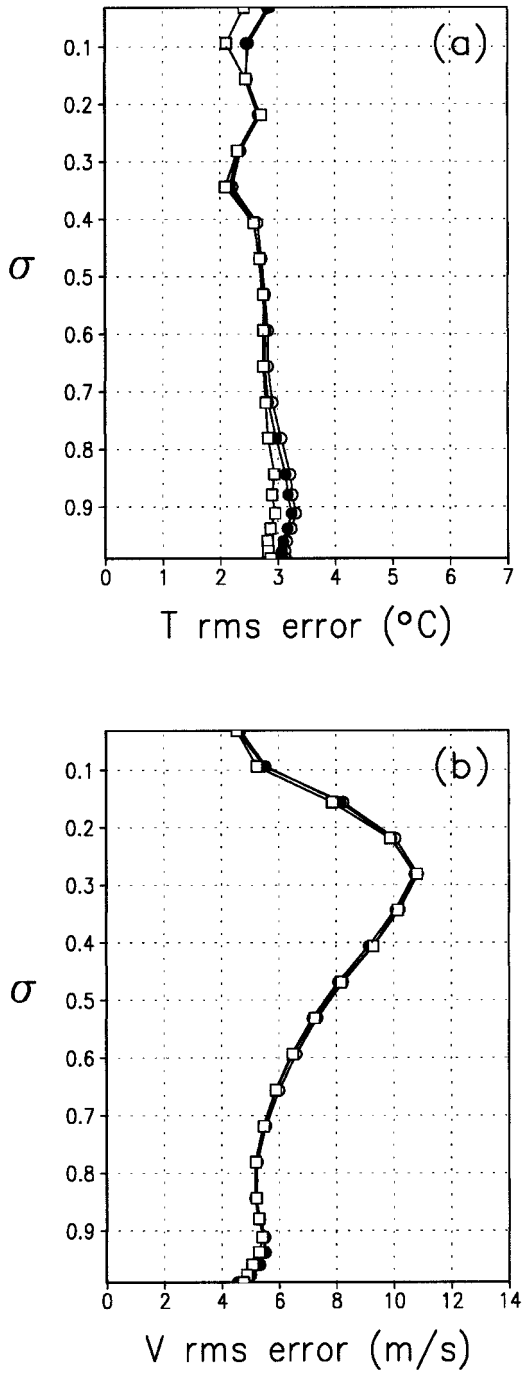

FIG. 4. Same as in Fig. 3 but with the corresponding biases extracted from the Utah model initialized with NCEP reanalysis (open circles) and ECMWF reanalysis (closed circles) and from the MRF (open squares).

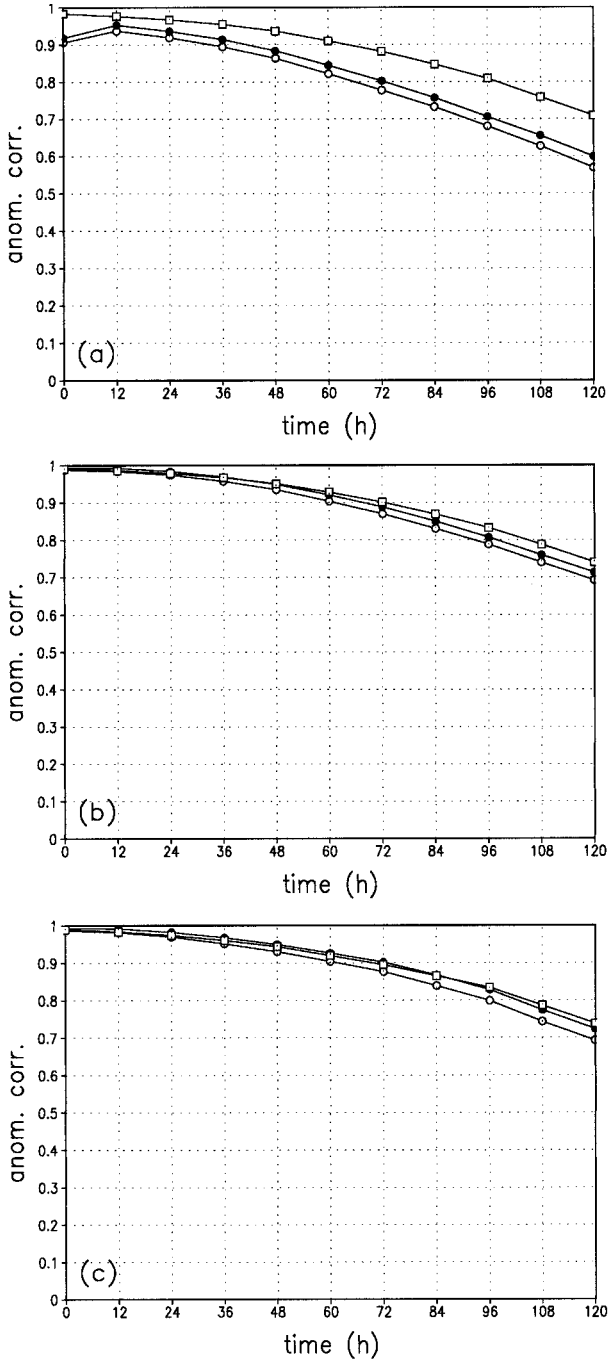

FIG. 5. (a) Time evolution of global, case-averaged anomaly correlations of the 500-mb geopotential height, for the Utah model initialized with NCEP reanalysis (open circles), ECMWF reanalysis (closed circles), and for the MRF (open squares). (b) Same as in (a) but with the corresponding biases removed. (c) Same as in (a) but for the Mar cases with the biases estimated a priori from the Jan and Feb cases.

March of 1993 is used to define climatology for this purpose. The MRF model clearly produces the highest anomaly correlations, and its skill at 120 h is similar to that of the Utah model at 96 h. The Utah model has slightly higher skill when initialized with ECMWF reanalyses than with NCEP reanalyses.

Skill scores can be improved by removal of bias, from both the Utah and MRF models as shown in Fig. 5b. The present bias correction is applied by extracting each model's average error from its individual forecasts using the 17-case average of the present forecast set. The bias-corrected MRF remains more accurate than the bias-corrected Utah model, and its skill at 120 h is similar to the bias-corrected Utah model skill at 114 h.

The model bias can also be calculated from an earlier ''training period'' and applied to subsequent independent cases. For example, the bias can be computed from the 12-case average error of January and February, and then applied to the 5 independent cases of March. The resulting, bias-corrected anomaly correlations for March (Fig. 5c) are similar to results of Fig. 5b.

2) Southern Hemisphere errors

The superior predictions from initializations using ECMWF reanalyses are due mostly to midlatitudes of the Southern Hemisphere. Figure 6a displays anomaly correlations computed over the latitude band from 65° to 25°S for a forecast initialized on 22 March 1993.

The curve with diamonds displays the anomaly correlation of the MRF model and has a value of about 0.64 after 120 h. The curves with open (closed) circles show anomaly correlations of the Utah model initialized with NCEP (ECMWF) reanalyses, respectively. The NCEP initialized forecast produces a 5-day anomaly correlation of 0.48, while the ECMWF initialized forecast produces an anomaly correlation of 0.69 at the same time.

The curves with open (closed) squares present anomaly correlations for experiments in which NCEP reanalyses are replaced by ECMWF reanalyses only within the global wavenumber range of 0–15 (16–42) at the initial time. Most of the beneficial impact of the ECMWF reanalyses in this example is apparently due to its longer-wave contributions.

Figure 6b illustrates southern midlatitude anomaly correlations for the same case after the bias (estimated a priori from the average error of the January and February cases) has been extracted. The impact of this correction is of similar magnitude as the impact of initial data selection, and the relative role of waves 0–15 is also evident in the bias-corrected results.

Figure 6c displays the southern midlatitude anomaly correlations (without bias correction) for the entire 17-case average. The MRF predictions are most accurate, the Utah model initialized with ECMWF reanalyses is superior to that initialized with NCEP reanalyses, and most of the benefit of the ECMWF reanalyses is due to the longer-wave contributions.

4. Global tests

The previous section concludes that most of the benefits of the ECMWF reanalyses relative to NCEP re-

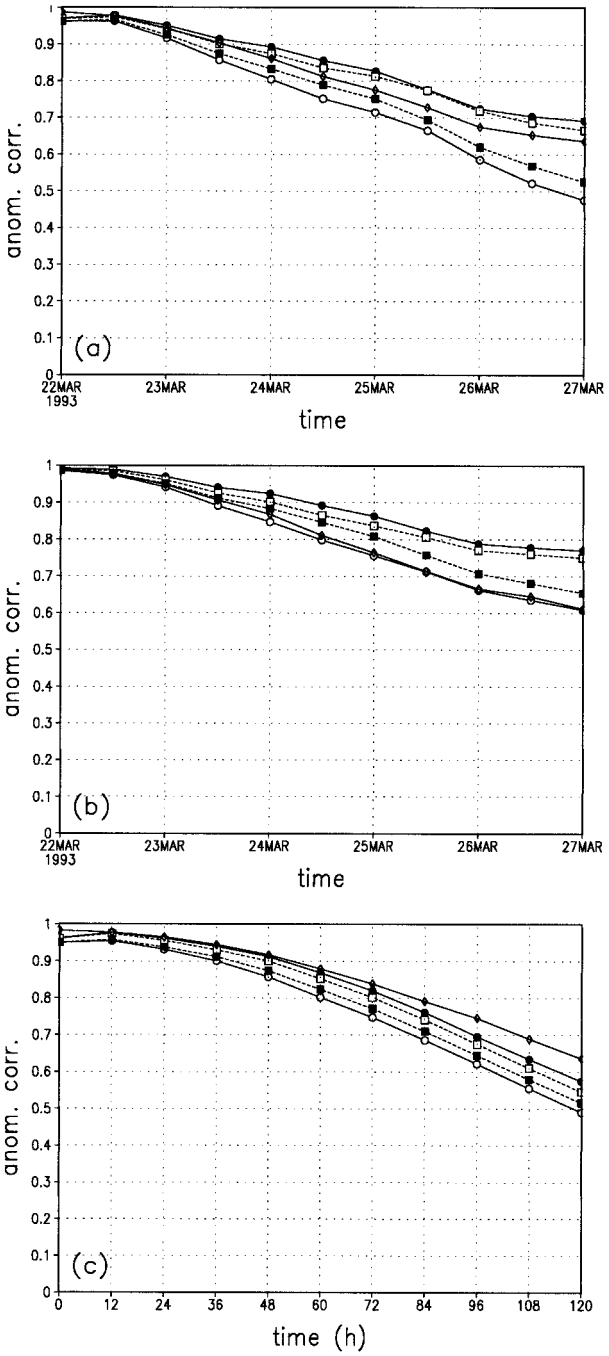

FIG. 6. (a) Time evolution of anomaly correlations of the 500-mb geopotential height, computed over the latitude band from 65° to 25°S for the case of 22 Mar 1993, of the Utah model initialized with NCEP reanalysis (open circles), ECMWF reanalysis (closed circles), and of the MRF (diamonds). Dashed curves with closed (open) squares denote results when ECMWF reanalyses are used only in global waves 16–42 (0–15) and NCEP reanalyses are used for the rest of the initial spectrum. (b) Same as in (a) but extracting the biases estimated a priori from the average error of the Jan and Feb cases. (c) Time evolution of anomaly correlations of the 500-mb geopotential height, computed over the latitude band from 65° to 25°S and averaged for the 17 cases. Curves as in (a) and (b).

analyses for Southern Hemisphere prediction are due to the longer-wave contributions. This disagrees with some initial state sensitivity arguments (e.g., Palmer et al. 1998; Hartmann et al. 1995), but is not inconsistent with other recent results (e.g., Barkmeijer et al. 1999).

Present conclusions are limited by several factors. The NCEP reanalyses incorporated subjectively analyzed surface data that proved to be erroneously placed in the Southern Hemisphere reanalyses (a phase shift of 180° longitude was discovered after the analysis was completed). This produced sizeable errors near the surface that decreased rapidly with height (J. Nogués-Paegle 1996, personal communication). The full impact of this error upon our results is unclear, since NCEP reanalysis surface pressures are used in both the NCEP and ECMWF initialized forecasts, but it is possible that some of the inferior Southern Hemisphere behavior of the NCEP initialized forecasts is due to this problem.

Anomaly correlations of geopotential height emphasize long-wave aspects of the initial state, because this field, and its analysis differences, maximize in wavenumbers 0–15. This is evident in the similar magnitudes of Figs. 1a and 2a. Because estimates of geopotential-based uncertainty emphasize longer waves, they may not adequately reflect the importance of shorter-scale contributions. By comparison, uncertainties of the wind field contain significant contributions from shorter wavenumbers, as may be noted in the different magnitudes of Figs. 1b and 2b.

Subsequent tests are evaluated from globally computed wind differences between the Utah model initialized with ECMWF and NCEP reanalyses. Global estimates minimize the relative contribution of possible analysis problems in higher latitudes of the Southern Hemisphere. On a global average, anomaly correlations produced by NCEP and ECMWF reanalyses differ by only about 0.02 (Fig. 5). Consequently, relative forecast errors are not good measures of sensitivity to initial state. In the present section, the sensitivity to initial state specification is estimated from the squared difference of meridional wind forecasts produced by model initializations with ECMWF and NCEP reanalysis data.

We emphasize the meridional wind component because forecast differences of this field reflect forecast differences of Rossby wave phase and amplitude. Variances (rather than rms values) of the difference field are computed since spectral contributions to the total variance are additive.

Figure 7 displays global variances of forecast meridional flow differences produced by initial data changes from NCEP to ECMWF reanalyses. Separate spectral wave groups are modified in the initial data, and results are normalized by dividing by the variance of the forecast meridional flow difference produced by initial state modifications of the entire spectrum. Figure 7a displays the impact of changing initial data only for global wavenumbers 0–5, 0–10, 0–15, and 0–20, denoted by curves with open circles, closed circles, open squares, closed squares, respectively. Figure 7b displays the impact of changing initial data only for the complementary wavenumbers 6–42, 11–42, 16–42, and 21–42, denoted by curves with open circles, closed circles, open squares, closed squares, respectively.

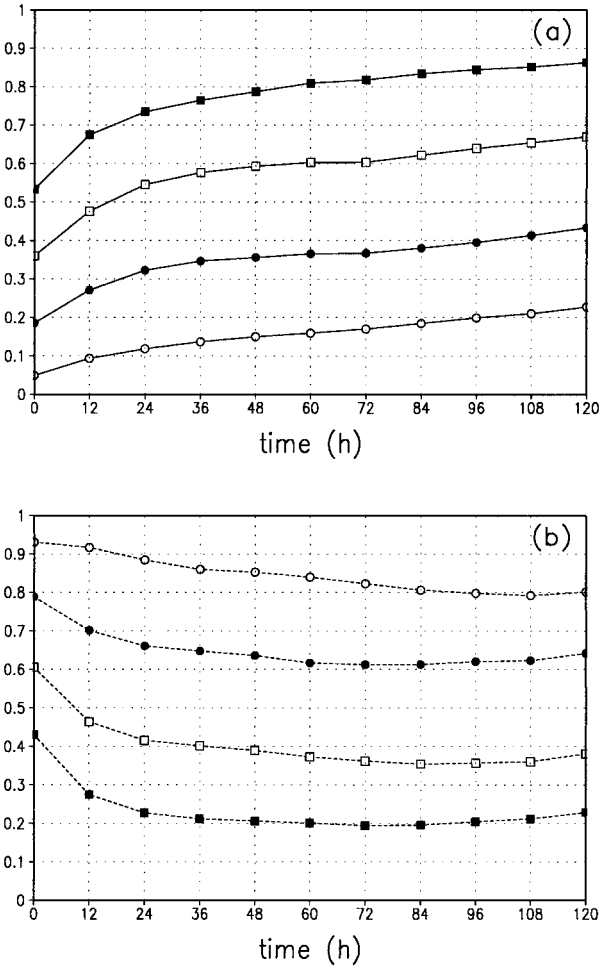

FIG. 7. Time evolution of global variances at $\sigma = 0.53$, of forecast meridional flow differences produced by initial data changes from NCEP to ECMWF reanalyses. Curves in (a) show the impact of changing initial data only for global wavenumbers 0–5 (open circles), 0–10 (closed circles), 0–15 (open squares), and 0–20 (closed squares). Curves in (b) display the impact of changing initial data only for the complementary wavenumbers 6–42 (open circles), 11–42 (closed circles), 16–42 (open squares), and 21–42 (closed squares). Results in both (a) and (b) have been normalized by dividing by the variance of the forecast meridional flow differences produced by initial state change of the entire spectrum.

The initial state analysis differences in wavenumbers 0–15 contain less than 40% of the total variance of the difference field at initial time, but produce variances in forecast differences equalling approximately two-thirds of the variance of the total difference field at 120 h. By contrast, the complementary experiment retaining initial state differences only in wavenumbers 16–42 contains slightly more than 60% of the initial variance, but describes less than 40% of the final total variance. The

initial state analysis differences contained in wavenumbers 0–20 produce more than 85% of the final total forecast difference in Fig. 7a, while the complementary cases retaining differences only in wavenumbers 21–42 produce only about 22% of the final total forecast difference.

If the forecasts were run over a much longer period error growth would eventually saturate, and all the curves in Fig. 7 would asymptote to 1. The fact that sums of complementary experiments approximately equal one rather than two suggests that the present experiments pertain to episodes of nearly linear error growth, which has not yet saturated.

Within this regime of unsaturated error growth the effect of changing long-wave components of the spectrum produces an error contribution that grows more rapidly in a relative sense than the effect of changing shorter-wave components of the initial state. This can be deduced from the systematic upward trend of curves in Fig. 7a and the downward trend of curves in Fig. 7b. The impact of wave groups 0–15 or 0–20 to 5-day forecast differences is substantially greater than the impact of the respective complementary shorter-wave groups.

Discussion

Results of Fig. 7 differ sharply from conclusions of several other recent studies. In particular, Palmer et al. (1998) and Hartmann et al. (1995) suggest that forecast error growth might be particularly effective for singular vectors which display an upscale growth. Most of the energy growth found by Hartmann et al. (1995) is produced by perturbations confined to the top half (high wavenumber end) of the total spherical harmonic wavenumber spectrum of singular vectors using a total energy metric both at initial time and at optimization time.

Snyder (1996) points out that sensitivity analyses should adequately reflect information about the analysis error. Recent singular vectors analyses that are consistent with estimates of analysis error statistics (Barkjeimer et al. 1999) differ considerably from singular vector analyses based solely upon an energy norm. The latter have a dominant wavenumber around 30, while the former have a dominant wavenumber around 10, and are more consistent with present results.

The total energy used in those analyses is based upon a metric of the form (e.g., Palmer et al. 1998; Barkmeijer et al. 1999; Hartmann et al. 1995, and others),

$$g_{ij}^{(\mathrm{ENE})} e^i f^j = \frac{1}{2} \int \left[\nabla \Delta^{-1} \zeta_{(e)} \cdot \nabla \Delta^{-1} \zeta_{(f)} + \nabla \Delta^{-1} D_{(e)} \cdot \nabla \Delta^{-1} D_{(f)} + R T_r \ln \pi_{(e)} \ln \pi_{(f)} + \frac{C_p}{T_r} T_{(e)} T_{(f)} \right] dv,$$

where $\zeta_{(e)}$, $D_{(e)}$, $\pi_{(e)}$, and $T_{(e)}$ represent, respectively, the vorticity, divergence, (log) surface pressure, and temperature components of the vector e^i (similarly for f^i), and the integration is performed over the whole volume of the atmosphere. Here, T_r is a reference temperature.

The aforementioned spectral estimates of forecast differences are founded upon spherical harmonic decomposition of the leading singular vectors (i.e., the most rapidly growing structures) in this norm.

Some of the differences of present conclusions with past results such as Palmer et al. (1998) and Hartmann et al. (1995) may reflect peculiarities of the presently used uncertainty measure. Figure 8 presents the spectral distribution of the average total energy of the initial and final ECMWF and NCEP initialized forecast difference (top panel) and the vertical distribution of the total energy associated with the difference field at initial and final time (bottom panel). Comparison of Fig. 8a with a similar estimate of energy of initial state differences given by Palmer et al. (1998, their Fig. 5a) shows a stronger decrease with total wavenumber in the presently used uncertainty measure. This may partly explain the relatively stronger long-wave impact of this study than that anticipated by Palmer et al. (1998).

A key weakness of present experiments is the use of differences between reanalyses as surrogates for analysis error. Since both reanalyses are based on (almost) the same data, the differences reflect mainly differences in forecast models and data assimilation schemes. In particular, the relatively low resolutions used in reanalyses may contribute to systematic errors in zonal means (see Fig. 16 of Simmons et al. 1995). This could explain part of the disagreement between the energy spectrum of analysis differences shown by Palmer et al. (1998) and Fig. 8.

Figures 9 and 10 present spectral and vertical distributions of the spectrum of total energy evolution (top panels) and of vertical distribution of total energy of the difference field (bottom panels). Figure 9 displays experiments in which the initial uncertainty is confined to wavenumbers 0–15 and Fig. 10 displays cases where this difference is initially confined to wavenumbers 16–42. The results differ substantially from analogous analyses presented by Hartmann et al. (1995, their Figs. 2 and 6), and also differ from analyses presented in Figs. 1b and 1d of Barkmeijer et al. (1999).

Figures 8–10 show 5-day amplification of initial differences of approximately 2 around wavenumber 10. In higher-resolution models, differences typically double more rapidly. One example of this can be found in the

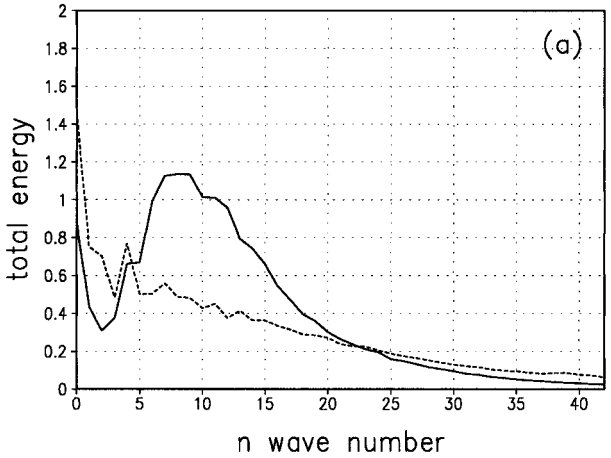

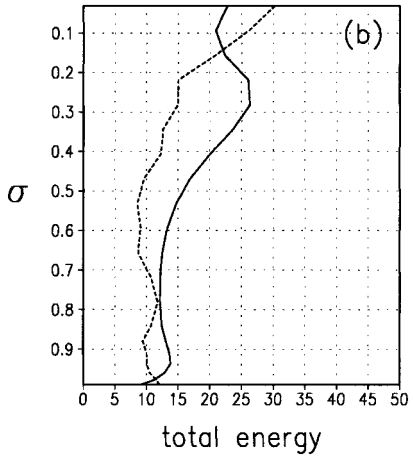

FIG. 8. (a) Spectral and (b) vertical distribution of the 17-case-averaged total energy of the initial (dashed) and final (solid) difference between ECMWF and NCEP initialized forecasts.

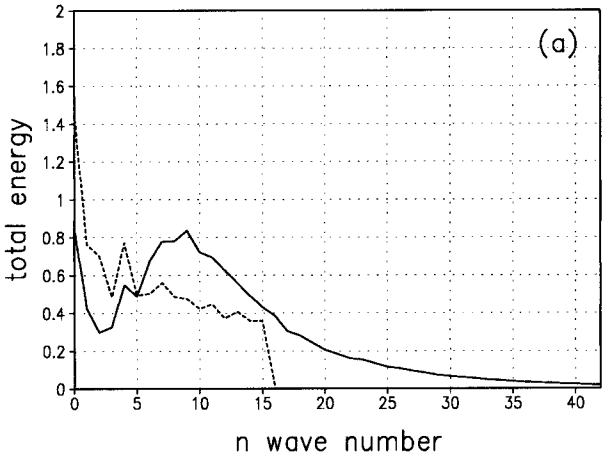

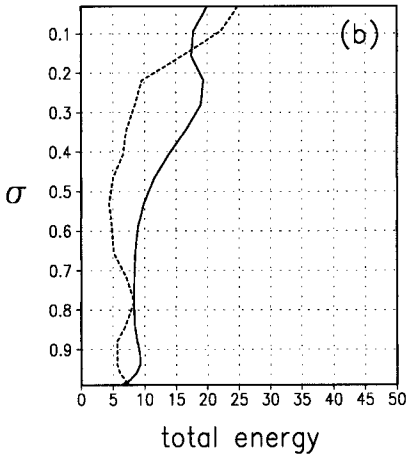

FIG. 9. (a) Spectral and (b) vertical distribution of the 17-case-averaged total energy of the initial (dashed) and final (solid) forecast difference between the experiment in which initial uncertainty is confined to wavenumbers 0–15 and the NCEP initialized control experiment.

solid curve of Fig. 17b of Rabier et al. (1996), which displays an exponential growth of initial state uncertainty up to day 2 or 3 in the 500-mb height field. In that study, initial perturbations are selected from the fast growing components of the error spectrum. In the present study, initial perturbations are retained in both growing and nongrowing structures, and much of the local perturbation structure damps similarly to analyses of Ehrendorfer and Errico (1995). The differences of 500-mb height forecasts initialized with ECMWF and NCEP reanalyses consequently start at larger values than that shown initially in Fig. 16b of Rabier et al. (1996), but the 5-day forecast differences are similar (results not shown). The present results may also be compromised by relatively low resolution in comparison to that used in other studies.

5. Conclusions

The present study concludes that initial state uncertainties possessing large spatial scale are more important than smaller-scale uncertainties for 120-h forecasts. This conclusion is consistent with idealized barotropic model studies by Thompson (1957) and Lorenz (1969) and with idealized baroclinic studies by Paegle et al. (1997). The present 17-case sample suggests that more than 40% of the final difference of a global data switch between NCEP and ECMWF reanalyses is obtained from the bottom fourth (wavenumbers 0–10), and almost 90% is obtained from the bottom half (0–20) of the spectrum retained by the present model.

The last conclusion contradicts results from Hartmann et al. (1995). They showed that when the initial perturbation is confined to the top half of the total spherical harmonic wavenumber spectrum (high wavenumber end), the growth rates and final structures of leading singular vectors are similar to the case in which all wavenumbers are included. Our conclusions do not question singular vector analyses; they only suggest that large-scale errors of the initial state may play a more

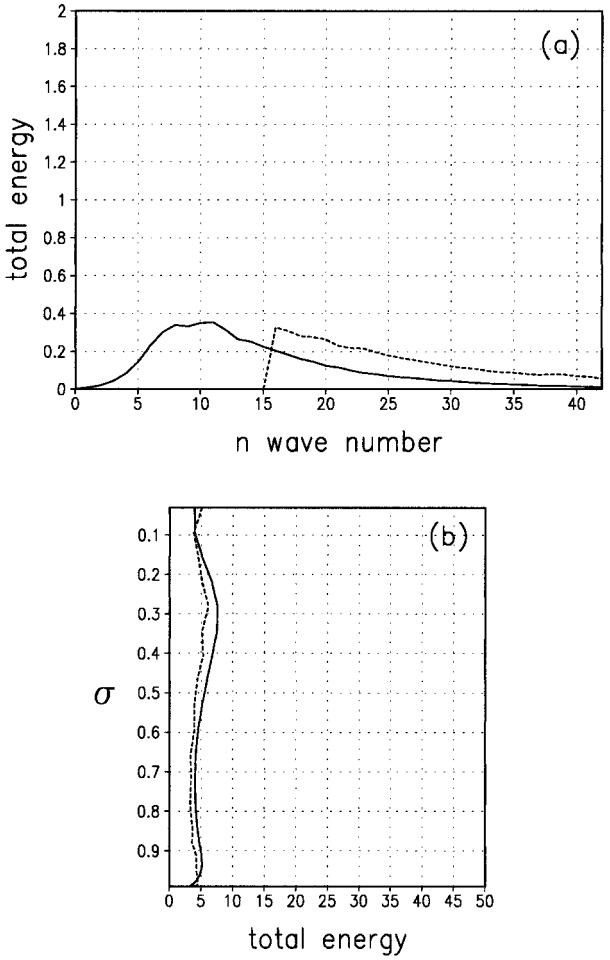

FIG. 10. (a) Spectral and (b) vertical distribution of the 17-case-averaged total energy of the initial (dashed) and final (solid) forecast difference between the experiment in which initial uncertainty is confined to wavenumbers 16–42 and the NCEP initialized control experiment.

prominent role than suggested in some singular vector analyses.

Present results are more consistent with the singular vector analysis of Barkmeijer et al. (1999) who include analysis uncertainty based upon the short-term forecast error of the model used in the analysis. Their results emphasize the importance of initial uncertainty around global wavenumber 10.

The apparent agreement with Barkmeijer et al. (1999) is not surprising given the present method of determining analysis uncertainty from the difference of two separate analysis methods. Both ECMWF and NCEP reanalyses use similar observations, and both methods partly fill observation voids by invoking a short-term forecast using respective (ECMWF and MRF model) short-term predictions. Part of the uncertainty estimate thus reflects different model forecasts, which may reflect model error.

Present conclusions are clearly limited by possibly nonrepresentative analysis error spectra and by the modeling method. We have used a research model that is still in development. It carries a bias that detracts about 1 day of predictive accuracy relative to the MRF model after 4–5 days. Most of this deficiency can be removed by a statistical extraction of the Utah model bias, but it is possible that conclusions may be different for different models.

Systematic misplacement of bogus surface data with a 180° longitude error in high latitudes of the Southern Hemisphere within the NCEP analysis system may also impact our results. The extent to which final conclusions are affected is unknown.

Perhaps the most important limitation of the present conclusions, and of many recent analyses of this problem, is the use of a forecast model truncated at wavenumber 42. This was done to allow a large number of forecast experiments (153 total forecasts in all) to be performed and stored. One case (not shown) was repeated at wavenumber 55 resolution, reducing latitude spacing from 2.2° to 1.8°. This showed larger error growth rates at all retained wavenumbers than the wavenumber 42 case, but the relative contributions of individual wave groups to the full spectrum was unaffected. The conclusions are sensitive to resolution because model diffusion increases with coarser resolution. Current operational models retain wavenumbers on the order of 100–200, and are characterized by significantly lower diffusion than used presently. It is possible that experiments at similarly high resolution may produce different results, and this remains an important area for future study.

Acknowledgments. This research was supported by NSF Grants ATM9714291 and ATM9423311 to the University of Utah. The reanalysis data were obtained from the National Centers for Atmospheric Research with assistance from Dr. J. Nogués-Paegle. Reviewer and editor comments led to major updates from an earlier manuscript, and Dr. Chris Snyder provided several useful suggestions.

REFERENCES

Barkmeijer, J., R. Buizza, and T. N. Palmer, 1999: 3D-var Hessian singular vectors and their potential use in the ECMWF ensemble prediction system. *Quart. J. Roy. Meteor. Soc.,* **125,** 2333–2351.

Buchmann, J., L. E. Buja, J. Nogués-Paegle, and J. Paegle, 1995: The dynamical basis of regional vertical motion fields surrounding localized tropical heating. *J. Climate,* **8,** 1217–1234.

Buizza, R., and T. N. Palmer, 1995: The singular-vector structure of the atmospheric general circulation. *J. Atmos. Sci.,* **52,** 1434–1456.

Charney, J. G., R. G. Fleagle, H. Riehl, V. E. Lally, and D. Q. Wark, 1966: The feasibility of a global observation and analysis experiment. *Bull. Amer. Meteor. Soc.,* **47,** 200–220.

Ehrendorfer, M., and R. M. Errico, 1995: Mesoscale predictability and the spectrum of optimal perturbations. *J. Atmos. Sci.,* **52,** 3475–3500

Errico, R. M., and T. Vukicevic, 1992: Sensitivity analysis using an

adjoint of the PSU–NCAR mesoscale model. *Mon. Wea. Rev.*, **120,** 1644–1660.

Gibson, J. K., P. Kållberg, S. Uppala, A. Nomura, A. Hernandez, and E. Serrano, 1997: ERA description. ECMWF Re-Analysis Project Report Series, Vol. 1, 58 pp.

Hartmann, D. L., R. Buizza, and T. N. Palmer, 1995: Singular vectors: The effect of spatial scale on linear growth of disturbances. *J. Atmos. Sci.,* **52,** 3885–3894.

Kalnay, E., and Coauthors, 1996: The NCEP/NCAR 40-Year Reanalysis Project. *Bull. Amer. Meteor. Soc.,* **77,** 437–471.

Kasahara, A., 1972: Simulation experiments for meteorological observing system for GARP. *Bull. Amer. Meteor. Soc.,* **53,** 252–264.

Lorenz, E. N., 1969: The predictability of a flow which possesses many scales of motion. *Tellus,* **21,** 289–307.

——, 1993: *The Essence of Chaos.* University of Washington Press, 227 pp.

Miguez-Macho, G., and J. Paegle, 1999a: Optimal observation distribution for numerical weather prediction. Preprints, *Third Symp. on Integrated Observing Systems,* Dallas, TX, Amer. Meteor. Soc., 18–23.

——, and ——, 1999b: Optimal observation distribution for numerical weather prediction. Preprints, *13th Conf. on Numerical Weather Prediction,* Denver, CO, Amer. Meteor. Soc., 23–26.

Mittelstadt, J. C., 1995: Sensitivity analysis using the adjoint equation of a quasigeostrophic model. Ph.D. dissertation, University of Utah, 155 pp. [Available from Dept. of Meteorology, University of Utah, Salt Lake City, UT 84112.]

Nicolini, M., K. M. Waldron, and J. Paegle, 1993: Diurnal variations of low-level jets, vertical motion and precipitation: A model case study. *Mon. Wea. Rev.,* **121,** 2588–2610.

Nogués-Paegle, J., K. C. Mo, and J. Paegle, 1998: Predictability of the NCEP–NCAR reanalysis model during austral summer. *Mon. Wea. Rev.,* **126,** 3135–3152.

Paegle, J., 1989: A variable resolution global model based upon Fourier and finite element representation. *Mon. Wea. Rev.,* **117,** 583–606.

——, and J. Horel, 1991: The influence of observational uncertainty upon wind-based analyses. Preprints, *Ninth Conf. on Numerical Weather Prediction,* Denver, CO, Amer. Meteor. Soc., 779–782.

——, Q. Yang, and M. Wang, 1997: Predictability in limited area and global models. *Meteor. Atmos. Phys.,* **63,** 53–69.

Palmer, T. N., R. Gelaro, J. Barkmeijer, and R. Buizza, 1998: Singular vectors, metrics, and adaptive observations. *J. Atmos. Sci.,* **55,** 633–653.

Rabier, F., E. Klinker, P. Courtier, and A. Hollingsworth, 1996: Sensitivity of forecast errors to initial conditions. *Quart. J. Roy. Meteor. Soc.,* **122,** 121–150.

Reynolds, C. A., P. J. Webster, and E. Kalnay, 1994: Random error growth in NMC's global forecasts. *Mon. Wea. Rev.,* **122,** 1281–1305.

Simmons, A. J., R. Mureau, and T. Petroliagis, 1995: Error growth estimates of predictability from the ECMWF forecasting system. *Quart. J. Roy. Meteor. Soc.,* **121,** 1739–1771.

Smagorinsky, J., 1969: Problems and promises of deterministic extended range forecasting. *Bull. Amer. Meteor. Soc.,* **50,** 286–312.

Snyder, C., 1996: Summary of an informal workshop on adaptive observations and FASTEX. *Bull. Amer. Meteor. Soc.,* **77,** 953–961.

Thompson, P. D., 1957: Uncertainty of initial state as a factor in the predictability of large scale atmospheric flow patterns. *Tellus,* **9,** 275–295.

Van den Dool, H. M., and S. Saha, 1990: Frequency dependence in forecast skill. *Mon. Wea. Rev.,* **118,** 128–137.

Vukicevic, T., 1998: Optimal initial perturbations for 2 cases of extratropical cyclogenesis. *Tellus,* **50A,** 143–166.

——, and J. Paegle, 1989: The influence of one-way interacting lateral boundary conditions on predictability of flow in bounded numerical models. *Mon. Wea. Rev.,* **117,** 340–350.

Wang, M., J. Paegle, and S. P. DeSordi, 1999: Global variable resolution simulations of Mississippi River basin rains of summer 1993. *J. Geophys. Res.,* **104,** 19 399–19 414.

Williamson, D. L., and A. Kasahara, 1971: Adaption of meteorological variables forced by updating. *J. Atmos. Sci.,* **28,** 1313–1324.